ADVANCED OPTICAL MATERIALS
www.advopticalmat.de

Near-Field Investigation of Luminescent Hyperuniform Disordered Materials

Nicoletta Granchi, Richard Spalding, Matteo Lodde, Maurangelo Petruzzella, Frank W. Otten, Andrea Fiore, Francesca Intonti, Riccardo Sapienza, Marian Florescu, and Massimo Gurioli**

Disordered photonic nanostructures have attracted tremendous interest in the past three decades, not only due to the fascinating and complex physics of light transport in random media, but also for peculiar functionalities in a wealth of interesting applications. Recently, the interest in dielectric disordered systems has received new inputs by exploiting the role of long-range correlation within scatterer configurations. Hyperuniform photonic materials, that share features of photonic crystals and random systems, constitute the archetype of systems where light transport can be tailored from diffusive transport to a regime dominated by light localization due to the presence of photonic band gap. Here, advantage is taken of the combination of the hyperuniform disordered (HuD) design in slab photonics, the use of embedded quantum dots for feeding the HuD resonances, and near-field hyperspectral imaging with sub-wavelength resolution in the optical range to explore the transition from localization to diffusive transport. It is shown, theoretically and experimentally, that photonic HuD systems support resonances ranging from strongly localized modes to extended modes. It is demonstrated that Anderson-like modes with high Q/V are created, with small footprint, intrinsically reproducible and resilient to fabrication-induced disorder, paving the way for a novel photonic platform for quantum applications.

1. Introduction

Whereas periodic structures with perfect translational symmetries display only a limited number of rotational symmetries, disordered and aperiodic geometries display statistical isotropies, which can lead to superior optical functionalities in many photonic applications, such as enhanced light extraction from light emitting diodes,[1] omnidirectional absorption for solar applications,[2] and random lasing.[3] In the last few years, disordered dielectric materials with structural correlations, which fill the gap between random structures and perfectly ordered photonic crystals, have generated an ever-growing interest.[4,5] A special class of these materials are the hyperuniform disordered (HuD) photonic systems.[6,7] HuD systems have recently been shown to display unconventional optical behavior such as transparency in thick optical media and large isotropic photonic band gaps (PBGs) comparable in width to band gaps found in photonic crystals,[8] as well as Anderson localization of light,[9,10,11] and their photonic properties are also statistically isotropic.[12–14] Pioneering experiments on photonic HuD systems have explored short-IR light diffraction in 3D dielectric structures,[15] polarization filtering,[16] and random quantum cascade lasers,[17] along with visible light scattering experiments from HuD plasmonic gold surfaces.[18] Also, theoretical proposals have been put forward for surface enhanced Raman scattering,[19] transparency design,[20] high-Q optical cavities and low-loss waveguides,[21,22] and microwave photonic circuits.[14] Still a quantitative experimental demonstration of the variety in light transport within a single HuD structure,

N. Granchi, F. Intonti, M. Gurioli
Department of Physics and Astronomy and LENS
University of Florence
Sesto Fiorentino (FI) 50019, Italy
E-mail: granchi@lens.unifi.it; massimo.gurioli@unifi.it

The ORCID identification number(s) for the author(s) of this article can be found under https://doi.org/10.1002/adom.202102565.

© 2022 The Authors. Advanced Optical Materials published by Wiley-VCH GmbH. This is an open access article under the terms of the Creative Commons Attribution-NonCommercial-NoDerivs License, which permits use and distribution in any medium, provided the original work is properly cited, the use is non-commercial and no modifications or adaptations are made.

DOI: 10.1002/adom.202102565

R. Spalding, M. Florescu
Advanced Technology Institute and Department of Physics
University of Surrey
Guildford, Surrey GU2 7XH, UK

M. Lodde, M. Petruzzella, F. W. Otten, A. Fiore
Department of Applied Physics and Institute for Photonic Integration
Eindhoven University of Technology
Eindhoven 5612 AZ, Netherlands

R. Sapienza
The Blackett Laboratory
Department of Physics
Imperial College London
London SW7 2AZ, UK

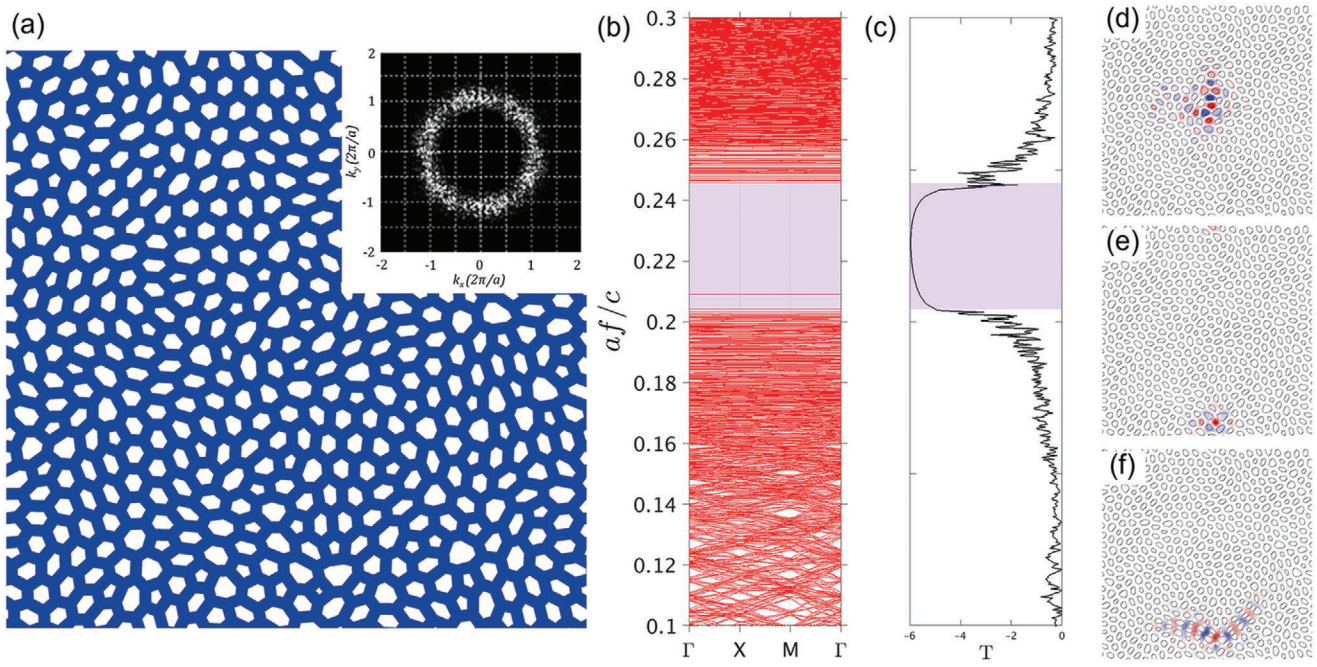


Figure 1. a) Sketch of the theoretical design of the studied hyperuniform disordered network, with length scale $a = 380$ nm and wall thickness $w = 0.46a$. The pattern contains 500 points. The inset shows the power spectral density of the structure (defined here as the magnitude square of the Fourier binary spatial dielectric distribution transform of the hyperuniform disordered network). b) 2D bandstructure (MPB) corresponding to the design in (a). c) 2D transmission spectrum. The purple stripe corresponds to the PBG. d–f) Magnetic field H_z (component normal to the plane) of bands 499, 500, and 501. Structure contours are shown as black lines.

with transition from PGB to Anderson-like localization,[23,24] to transport regimes such as diffusive multiple scattering is still missing in the optical range.[25] In this article, we directly measure the transition from localization to diffusive transport within a single system by exploiting near-field mode imaging capable of sub-wavelength resolution in the near-IR range. To this end we are employing a special design of HuD in slab photonics with embedded quantum dots for feeding the HuD resonances via photoluminescence. The use of near-field hyper spectral imaging (HSI) with sub-wavelength resolution allowed us to perform a statistical analysis of individual many photonic modes, determining their Q factor, inverse participation ratio (IPR), mode volume V, and areal density. We theoretically predict and experimentally demonstrate that photonic HuD systems support a variety of transport regimes as well as a PBG. We also show that high Q factor and small mode volume resonances are created in strong similarity to photonic crystal cavity but with the advantage of having a very small footprint. Eventually, these modes turn out to be intrinsically reproducible, with the mode spatial distribution robust against fabrication-induced disorder.

2. Theory and Design

We begin our analysis with the study of a purely 2D HuD network system (shown in **Figure 1**a), generated with a protocol described in ref. [7] and reviewed in the Experimental Section. Analogously to the lattice constant in photonic crystals, we define a length scale $a = L/\sqrt{N}$, such that an N-point hyperuniform pattern in a square box of side length L has a scatterer density of $1/a^2$. The point pattern we use contains $N = 500$ points and belongs to a further sub-category of HuD systems, known as "stealthy,"[9,26] whose name relates to their property of being transparent to incident radiation for a certain range of wavevectors k. In particular, we consider a stealthy point pattern with a structure factor $S(k)$ that is statistically isotropic, continuous, and precisely equal to zero for a finite range of wavenumbers smaller than a certain wavevector k_c, that is, $S(k < k_c) = 0$. The stealthiness parameter χ is defined as ratio between the number of k vectors for which the structure factor $S(k)$ is constrained to vanish and the total number of k vectors, as shown in the inset of Figure 1a, the resulting HuD structure preserves this property and the power spectral density of the structure (defined here as the magnitude square of the Fourier binary spatial dielectric distribution transform of the HuD network) vanishes for a circular domain centered around the origin. A summary of the main properties for a system with $\chi = 0.5$ and $a = 380$ nm is given in Figure 1; the index of refraction is set to $n = 3.4$, and thickness of the dielectric veins (the network wall thickness) is $w = 0.46a$. The 2D photonic bandstructure reported in Figure 1b is calculated using the planewave expansion software MPB.[27] The PBG (purple region) is not affected by the folding and is located between bands (red lines) N and $N + 1$, where N is the number of scattering cells in the supercell, in this case $N = 500$. The transmission spectrum (Figure 1c) is obtained via FDTD methods (details in Experimental Section). The resulting transmission spectrum and 2D bandstructure are in very good agreement; the clear suppression of the transmission over a range of frequencies indicates the presence of a PBG, as predicted by the bandstructure calculations. Like other conventional disordered

© 2022 The Authors. Advanced Optical Materials published by Wiley-VCH GmbH

structures, unperturbed HuD structures display spatially localized modes. These Anderson-like localized modes occur naturally at the PBG edges and are predicted to spread over a few cells of HuD network structures.[21,28]

Calculation of the HuD network's bandstructure with MPB offers information on both the frequency and spatial distribution of the modes. By itself, the spatial extent provides useful knowledge on the wave transport process. In Figure 1d–f, we report the distributions of the magnetic field component normal to the xy-plane, H_z, of bands 499, 500, and 501, respectively. These modes are archetypal examples of the main features of HUD; interestingly, mode 500 (corresponding to the most isolated band inside the gap in Figure 1b), is an accidental defect mode arising due to local peculiar topology[28] on the four-sided cells; we note that most of the cells in the structure are surrounded by five, six, or seven sides with an average of six sides per cell. The accidental defects are quite rare but unavoidable; more details can be found in Section S1, Supporting Information. The defect modes associated with them are most often located around the lower edge of the PBG, and they represent an interesting peculiarity of HuD. Mode 499 is the first localized mode in the dielectric band, while mode 501 is the first localized mode of the air band. This means that the difference between them, in terms of frequency, defines the side of the HUD-PBG. In addition, they are easily distinguishable as below (Figure 1d) or above (Figure 1f) the PBG due to the electric field being concentrated in the dielectric or air fraction, respectively.

The physical reason is that below the band gap, TE modes concentrate the magnetic field inside the air fraction (electric field concentrated in the dielectric material) so as to reduce the electromagnetic energy functional.[13] Above the gap, due to the requirement that solutions to the Maxwell–Eigen problem are orthogonal, the magnetic field is pushed into the dielectric material as nodes form in the air fraction; this is a well-understood paradigm in periodic structures[29] that can be observed also in HuD systems. The method of wave transport can also be inferred from the field profiles. Low-frequency modes have an extended profile that suggests ballistic propagation; the structure has limited influence on the mode profile. For higher frequencies, the modes become much more localized; the band-edge modes are confined to within just a few cells due to Anderson localization.

Consequently, in hyperuniform systems the quality factors for the low-frequency modes are low and increase approaching the band gap. The field profiles of these modes echo the nature of the transition in the wave transport of the modes. Low-frequency modes have extended field profiles, with the electromagnetic energy quickly leaking out through in-plane directions. On the other hand, localized modes are confined, their decay is therefore slower and their quality factors higher. Resonances in close spectral proximity to the PBG have very large Qs relative to other modes, owing to Anderson-like localization confinement in the plane of structuring.

The mode profiles shown so far are calculated for a structure with infinite extent in the vertical direction, that is, a 2D simulation. For an in-plane slice at the vertical center of a 3D slab with the same design, we expect to find a very similar field profile to the mode's 2D counterpart, just at a higher frequency. As a result, from the 2D field profile of a band-edge mode, we can deduce the exact band-edge frequency of the 3D slab. By monitoring the evolution of the in-plane field with time, we obtain the electric field profiles of three selected modes of the 3D HuD network slab as presented in **Figure 2**a–c, together with the corresponding Fourier transforms in Figure 2d–f (details on the calculation process can be found in Section S2, Supporting Information). From the profile of their Fourier transforms, is evident that these three modes are well confined in the vertical direction, with most of the reciprocal space components located outside the light cone. In particular, Figure 2a,d is relative to a typically delocalized mode (band 479, $\lambda = 1349$nm) with a Q factor of 920, which is much lower than the Q factor of the localized mode at the band edge in Figure 2b,e (band 499, $\lambda = 1310$nm) displaying a Q factor of 4200. Figure 2c,f display the behavior of the fourfold accidental defect (band 500, $\lambda = 1280$nm): this mode displays a lower Q factor (750) despite the tighter in-plane spatial confinement, due to the losses in the vertical direction associated with the k-space components inside the light cone and directly related to the symmetry and the spatial extent of the intensity profile.[21]

3. Experimental Results

The sample investigated is a HuD dielectric structure on two GaAs parallel membranes with air holes following the network pattern of Figure 1a. The vertical etching ensures that the hole patterns in the two parallel membranes have the same nominal design. Double-membrane photonic systems have been recently proposed as novel devices for sensing and metrology applications, based on the achievement of deterministic control of the supported modes.[30–33] **Figure 3**a shows the top view scanning electron microscopy (SEM) image of one of the investigated samples, with nominal lattice constant $a = 380$ nm and wall thickness $w = 0.46a$. The near-field analysis is done by photoluminescence with a commercial scanning near-field optical microscope (SNOM) in an illumination/collection geometry. Further experimental details on the sample fabrication and near-field imaging are given in Experimental Section.

The spatially resolved optical maps were recorded by scanning the probe tip over the sample at a fixed distance (few tens of nm), and this technique allows us to perform HSI, that is we collect a full spectrum of the photonic local density of states (LDOS) of a system for any spatial pixel of the near-field map. The quantum dots (QDs) PL emission spectrum is reported in the inset of Figure 3b, and by design it is spectrally overlapped to modes at the lower PBG edge. In order to achieve insight into the nature of the photonic modes, for every tip position, we calculate the PL enhancement spectrum by dividing the recorded near-field spectrum by the one of the QDs (see Figure S3, Supporting Information). The graph of Figure 3b is a typical PL enhancement spectrum (i.e., the photonic LDOS[33]) acquired on a broad range of wavelengths at a specific probe position. The detected resonances are spectrally sparse over the full emission of the QDs. The experimental data clearly define three main regions, according to what theory predicts: region 1 (1100–1160 nm) is characterized by the effect of the PBG with no detected modes. The very first resonances appear around 1160 nm, showing strongly localized field profiles (similar to

© 2022 The Authors. Advanced Optical Materials published by Wiley-VCH GmbH

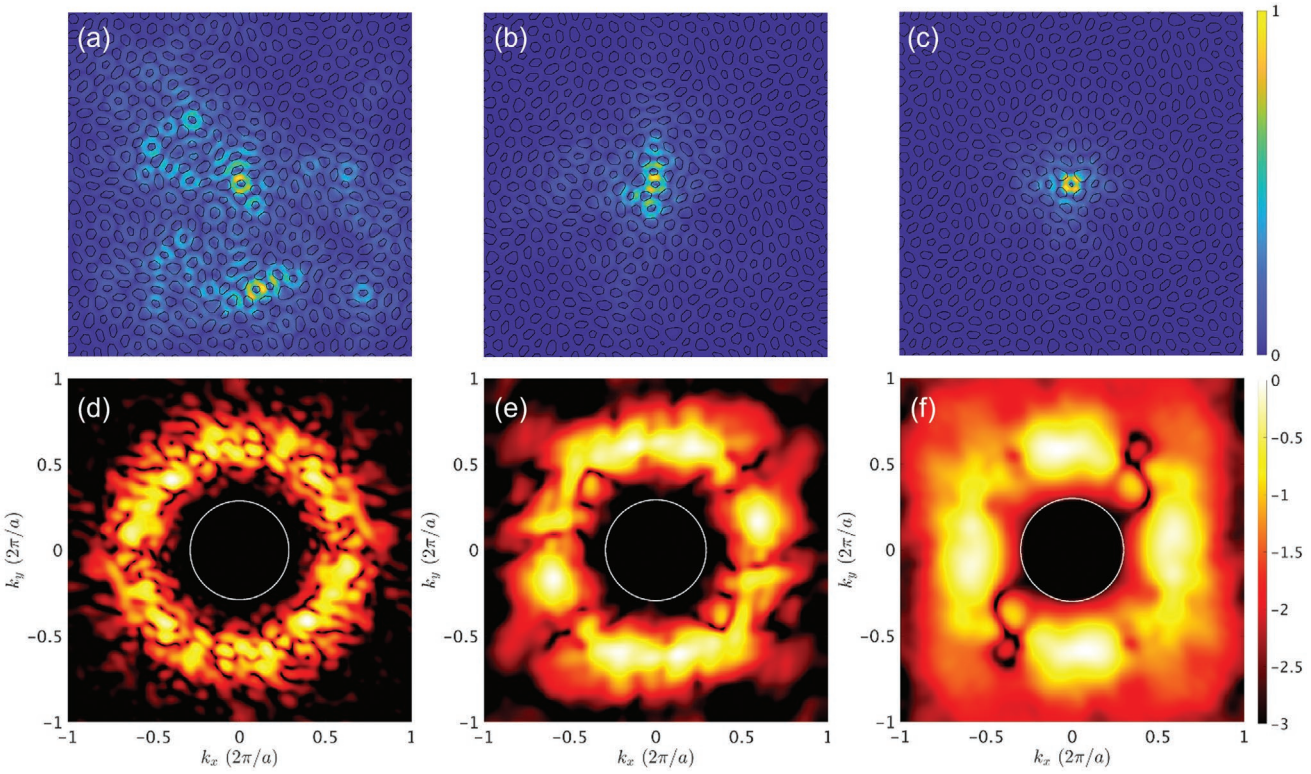


Figure 2. FDTD electric field intensity profile ($|E|^2$) of band a) 479, b) 499, and c) 500 modes, respectively. Note that mode 500 has been translated at the center of the simulation window. d–f): Fourier transform of the magnetic fields that correspond to the electric field intensity profiles in (a), (b) and (c), respectively; the light cone in each case is indicated by the white circle.

the one in Figure 2b); this feature is shared with all modes within region 2 (1160–1195 nm). Then, increasing the wavelength, after a transition region (1195–1225 nm), the modes show a delocalization over the whole structure (similar to the one in Figure 2a), and we named this region 3 ($\lambda > 1225$ nm). The near-field imaging gives direct access to the spatial extension of the HuD modes, allowing us to study the details of the transition between localized and delocalized modes near the dielectric band edge. This can be quantitatively measured by calculating the IPR,[34–36] which is defined as

$$\mathrm{IPR} \equiv \frac{\int |E(r)|^4 \, dr}{\left(\int |E(r)|^2 \, dr\right)^2} V_{\mathrm{tot}} \tag{1}$$

where $|E(r)|^2$ is the intensity distribution of the electric field in the eigenstate and V_{tot} is the total volume of the system. Values of IPR close to one indicate the electric field intensity being constant throughout the system volume, while higher values are associated with the intensity confined to a small volume. In Figure 3c, we show the trend of the theoretical and experimental calculation of the HuD modes with respect to the wavelength λ; the blue dots represent the values obtained by finite element method (FEM) simulations, while the red dots are relative to the results extracted from the SNOM experimental data.

Details on the simulations and the experimental fits can be found in Experimental Section and in Sections S3–S7, Supporting Information. Note that there is a wavelength shift of 15 nm between measurements and simulations, which is to be attributed to uncertainties on the structural parameters of the real sample (See Section S4, Supporting Information). It is also worth noting that a value of IPR of the order of 13 is considered as the threshold (represented by the horizontal green dashed line in Figure 3c) above which the modes become localized, and it corresponds to a localization length[9] of the order of 2 μm. Following this threshold, we demonstrate the presence of two regions with only localized (2) or delocalized (3) modes; the transition region between the two (and therefore the spectral position of the vertical dashed lines) is defined as the spectral window were modes with IPR greater and smaller than 13 are both present. This region is very interesting, likely describing the coexistence between localization and diffusive transport. The theoretical values are in good agreement with the experimental data. Furthermore, in Figure 3d,e we report the SNOM map of a typical localized (delocalized) resonance at $\lambda = 1190$ nm ($\lambda = 1260$ nm), reconstructed from the fitted amplitude of the mode (more details in Sections S5–S7, Supporting Information). We remark that the PL signal is mostly localized into the dielectric, as predicted by simulations for the electric field intensity of modes below the band gap.

An interesting theoretical prediction is that HuD modes may have high quality factors when localized and close to the PBG, while the Q decreases for extended modes far from the band edge. This trend is well represented in Figure 3f, in which we show the theoretical Q values (green dots), together with the experimental fitted values (red dots) obtained by near-field PL.

© 2022 The Authors. Advanced Optical Materials published by Wiley-VCH GmbH

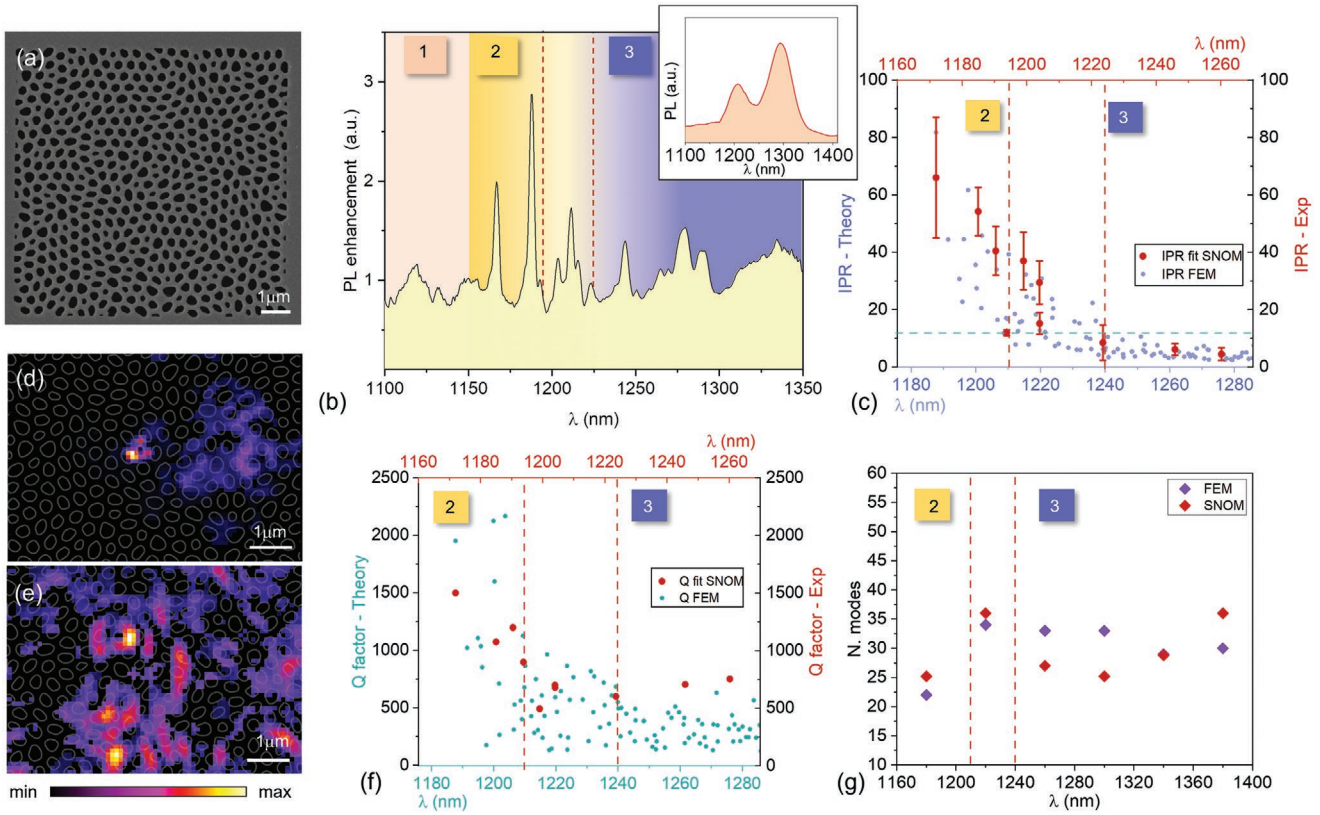


Figure 3. a) Scanning electron microscopy (SEM) image showing the top view of the sample. b) Typical PL enhancement spectrum at a given tip position on a broad wavelength interval. Labels 1, 2, and 3 indicate the PBG spectral region and the spectral intervals in which localized (2) and delocalized (3) modes are detected, respectively. The transition spectral window between regions 2 and 3 is indicated by red dashed lines. The inset displays the QDs PL emission spectrum. c) Evolution of IPR with respect to the wavelength as a description of light localization for experimental values (red dots, calculated by using the fitted amplitude maps of the selected modes) and eigenstates of the SEM-design structure (blue dots) obtained with FEM simulations. The green dashed horizontal line indicates the threshold of IPR = 13, while the red dashed vertical lines highlight the transition window from region 2 to region 3. The error bars in the experimental data are estimated as the maximum deviation between the minimum and maximum acceptable values of the IPR obtained by changing the threshold of the fits. d,e) SNOM fitted amplitude maps of a localized mode ($\lambda = 1190$ nm) and of a delocalized mode ($\lambda = 1260$nm), respectively. f) Theoretical Qs (green dots) and experimental Qs (red dots) calculated from fit with respect to the wavelength. No error bars are reported since, because of the spectral resolution (0.11 nm per pixel), they would not be visible in the graph. g) Number of modes for different spectral regions calculated with FEM simulations (purple diamonds), and extracted from the SNOM measurements (red diamonds).

The experimentally detected resonances are characterized by quality factors ranging from 1500 to 500 and reproduce well the theoretical trend. In order to obtain a full characterization of the physical properties of HuD modes, we address the relation between cavity mode volume and the rate of spontaneous emission[37] by evaluating the modal volume V[38] (details of the calculation are reported in Section S6, Supporting Information). We obtained an experimental value of $V \approx 0.06$ μm^3 for the most localized mode at the PBG edge, which is comparable with the modal volume of an L3 cavity, $V \approx 0.07$ μm^3.[39] Clearly, HuD modes located in the band gap vicinity are characterized by a high ratio Q/V (of 25 000 μm^{-3}), suggesting their exploitation for quantum electrodynamics (QED) effects.[40,41] Within this context, a relevant aspect is the evaluation of the areal density of HuD modes. We complete the statistical analysis of the modes by giving an indication of the numerical density of modes with respect to the wavelength; we count the total number of photonic modes of the HuD structure detected in an 8 μm × 8 μm scan by dividing the spectral range into six intervals. The summary given in Figure 3g shows that the number of modes determined experimentally (red diamonds) is in good agreement with the theoretical predictions from FEM simulations (purple diamonds) (full details on the analysis of the mode counting are given in Section S3, Supporting Information). It is worth noting that there are more than 50 HuD modes with high Q/V in a spectral region of 80 nm; this is much higher when compared to photonic crystal cavities, where in the same sample area usually only one cavity (with two or three modes) is designed.

To further explore the assessment of the suitability of HuD for QED effects, we exploit the HSI technique as a powerful tool to obtain, for every peak of a spectrum, the corresponding spatial profile. In order to present a comprehensive picture of the collective mode distributions, we report a map of the maximum PL enhancement measured at each SNOM step within a broad spectral region (1165–1280 nm) in **Figure 4**a. We note that this map is neither a single-mode map, nor a map at a single emission frequency: it is a collective map, where each bright spot refers to the brightest mode (or superposition of modes) in that spatial region, within the selected spectral

© 2022 The Authors. Advanced Optical Materials published by Wiley-VCH GmbH

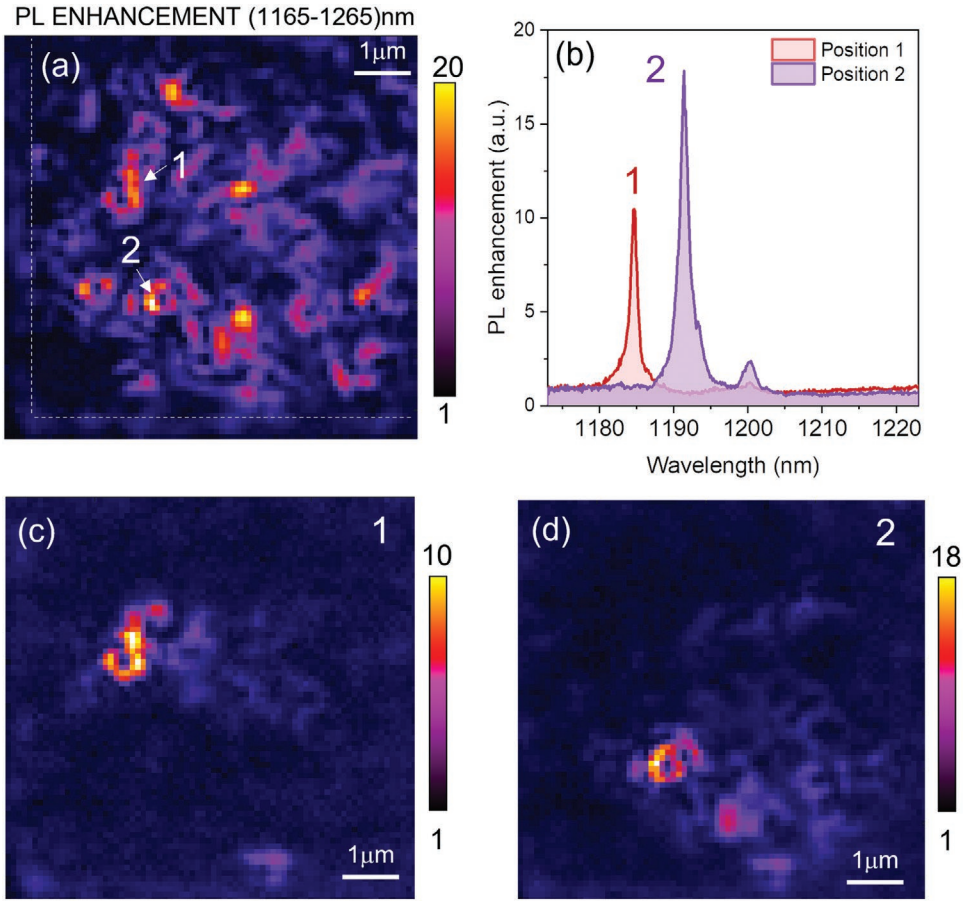


Figure 4. a) Map of the maximum PL enhancement in the spectral region (1165–1265 nm), extracted from a SNOM PL map of 8 μm × 8 μm, with a scanning step of 100 nm per pixel. 1 and 2 indicates the positions where the red and purple spectra, reported in (b) were acquired. c,d) show the PL enhancement maps filtered around the central wavelengths of peaks 1 and 2, $\lambda = 1184.7$ nm and $\lambda = 1191.4$ nm.

window. Therefore, it can be used as an indication of the position of the localized modes. We observe many modes distributed over the whole patterned area, indicating there is a high spatial density of modes, as reported in Figure 3g. Most of these modes exhibit a PL enhancement of the order of 20, a value that is double the typical enhancement factor of recently studied random modes.[33] Figure 4b shows two typical mode resonances in two different positions of the map (1 in red and 2 in purple) that display some of the several sharp resonances found in the structure. These peaks reveal a Q factor of 1000 and 600, respectively, and are spectrally well isolated. The corresponding spatial profiles are reported in Figure 4c,d, filtered around $\lambda = 1184.7$ nm and $\lambda = 1191.4$ nm, denoting a modal volume of 0.06 μm^3 and 0.08 μm^3.

The high Q/V ratio, as well as the large areal density displayed by HuD resonances near the PBG edge make them appealing as a promising platform for QED applications. A further important aspect in this perspective is the mode predictability for the design and their robustness against fabrication-induced disorder. Here, these aspects have been explored both experimentally and theoretically. Specifically, we designed two nominally identical samples and demonstrated that the same modes can be observed in the two samples; an example is given in **Figure 5**. In particular, we exploit the combination of HSI near-field mapping with topographic imaging of the sample for aligning different maps at the nanoscale. In Figure 5a we present the spectrum acquired at the position of maximum intensity of the PL signal of the mode of the replica (in blue), compared with respect to its counterpart in the original structure (in green). Correspondingly, Figure 5b,c show the SNOM PL maps acquired at the central wavelengths of the two peaks, $\lambda = 1203.3$ nm and $\lambda = 1204.6$ nm, respectively. Despite the fabrication disorder-induced 2 nm shift between the two resonances, the similarity of the sub-micrometric details in the field distributions of the two replicas is evident, not only in the brightest spots, but even throughout zones with a lower signal. This provides a clear demonstration of the modes' robustness with respect to unavoidable fabrication-induced disorder. A further proof of the mode robustness is provided by numerical simulations; here, we compare the mode profiles obtained from the nominal design and the real dielectric pattern generated from the SEM image of the sample ("SEM-design"). Again, we find that the spatial profiles of the strongly localized modes are almost unchanged. As an example, two FEM simulated maps for the first mode of the dielectric band (band 499) obtained with the nominal theoretical pattern and the SEM-design: the maps are reported in Figure 5e,f, respectively ($\lambda = 1203.7$ nm and $\lambda = 1187.0$ nm). Despite a spectral shift of almost 17 nm, the

© 2022 The Authors. Advanced Optical Materials published by Wiley-VCH GmbH

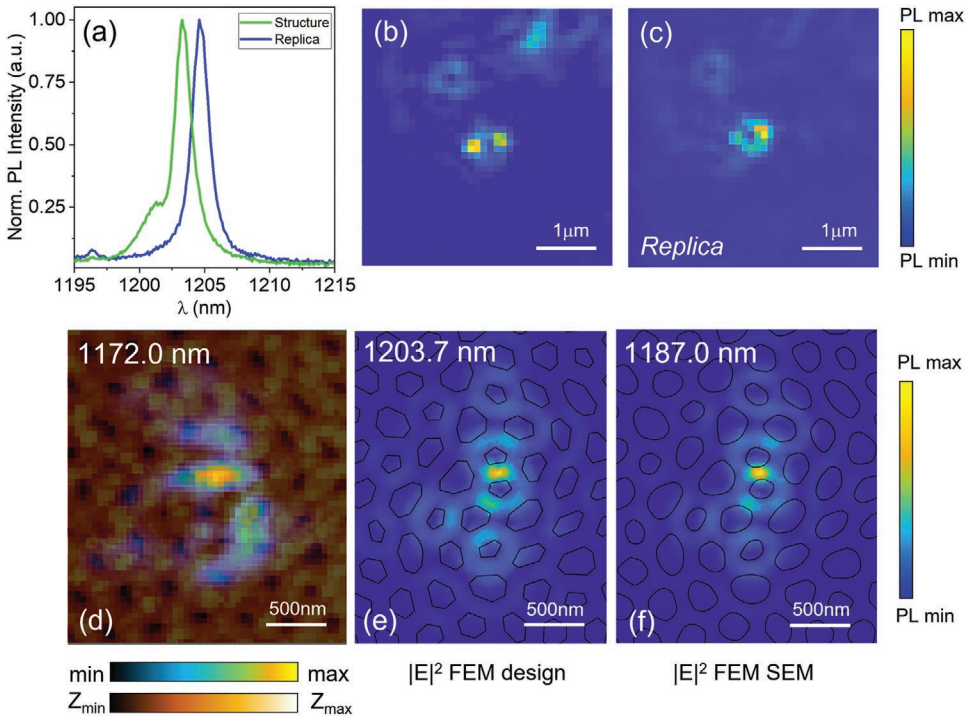


Figure 5. a) PL spectrum of the same mode in two nominally identical replica (green and blue), acquired in the point of PL maximum intensity in the maps of (b) and (c), respectively. b,c) Near-field PL maps at $\lambda = 1203.3$ and $\lambda = 1204.6$ nm of the two nominally identical samples. d) Fitted amplitude map of mode 499, overlapping the SNOM topography. The two color bars are, respectively, related to the map of the fitted amplitude and the topography. In the first, yellow corresponds to the maximum amplitude, and black to the minimum but it is not visible due to the transparency. In the second, black (white) corresponds to the minimum (maximum) z position of the tip, and this is why the holes are in black. e,f) FEM electric field intensity map of mode 499 obtained from the simulation of a double-membrane system patterned e) with the nominal design and f) with the SEM design.

smoothing of the holes, and the slightly altered morphology of the network, the electric field of the mode preserves the most important features that characterize its spatial footprint, that is, unaltered locations of intensity hotspots and spatial localization over few cells from the center of the mode. These are also compared with the SNOM fitted amplitude map (Figure 5d), which agrees very well with the theoretical predictions. A full description of the FEM simulation processes, along with examples of modes detected in theory and experiment, are reported in Section S7, Supporting Information; further quantification of the robustness of HuD modes with respect to disorder is presented in Section S8, Supporting Information, where we compare the response to local disorder of the band 499 mode and a conventional mode of a random structure.[33]

Our results provide a clear demonstration that despite the disordered character of the HuD structures, the introduction of hyperuniformity and the presence of a PBG makes these photonic structures robust against unavoidable fabrication-induced disorder.

4. Conclusions

In summary, by employing a near-field optical analysis at telecom wavelengths we have demonstrated that HuD photonic systems combine localized and delocalized modes. This brings together the advantages of both disordered systems and ordered systems. More strikingly, next to the high spectral and spatial density typical of random modes, which could allow the long-lasting problem of spatial and frequency matching between exciton and photon to be overcome, the hyperuniform resonances exhibit higher PL enhancement factor, Q factors one order of magnitude higher than typical random photonic systems (1500 experimentally detected), and modal volumes comparable with the best PCs, due to the localization of light of modes that occur near the PBG edges. Remarkably, our HSI experiment allowed us to demonstrate, in agreement with theoretical simulations, the possibility of detecting different light transport regimes through the analysis of the spatial profiles of the modes and the exploration of light localization and delocalization in a system whose structuring place at the junction between fully ordered and completely random systems. We addressed the physical nature of the detected resonances, going from Anderson-like resonances to more delocalized regimes, by describing important statistical properties, all sharing the fascinating feature of intrinsic reproducibility and resilience to fabrication-induced disorder. Our results open routes yet to be explored for addressing basic physics and practical applications of hyperuniform materials, combining the advantages of both ordered and disordered systems.

5. Experimental Section

Sample Design: The sample was a system of two parallel GaAs membrane, patterned with a stealthy HuD network design with

© 2022 The Authors. Advanced Optical Materials published by Wiley-VCH GmbH

stealthiness $\chi = 0.5$, length scale $a = 380$ nm, and wall thickness $w = 0.46$. 2D hyperuniform point patterns were disordered point patterns for which the number variance $\sigma^{(2)}(R)$ in a circular sampling window of radius R grew more slowly than the window area for large R. The point patterns used in this work were also stealthy, that is, their structure factor $S(k)$[6] was defined as

$$S(k) = \frac{1}{N}\left\langle \sum_{i,j=1}^{N} e^{ik(r_i - r_j)} \right\rangle \quad (2)$$

where k are vectors in reciprocal space, N is the total number of particles, $r_{i,j}$ are the positions of ith and jth particles and $\langle\ \rangle$ denotes ensemble average. In this work, the forward scattering contribution is omitted, that is, the reduced scattering factor $\tilde{S}(\boldsymbol{k}) = S(\boldsymbol{k}) - (2\pi)^2\,\delta(k)$ was considered. For HuD stealthy point patterns, $\tilde{S}(\boldsymbol{k})$ was statistically isotropic and was zero for a range of k-values, $0 < k \leq k_0$, for some positive critical wave vector, k_0.[36] The degree of hyperuniformity was them measured by the stealthy hyperuniform order parameter $\chi = M(k)/(2N)$, where $M(k)$ is the number of linearly independent k vectors with $0 < k \leq k_0$ for which $S(k) = 0$ and $2N$ is the total number of degrees of freedom for the 2D point pattern.

To generate 2D stealthy hyperuniform point patterns, the collective coordinate method was employed.[42] To minimize the finite size effects, the point patterns of fixed number of points N and hyperuniformity χ were generated in a square of size L under periodic boundary conditions.[20,43,26]

In the case of HuD structures, it was shown that the largest PBG for TE-polarized modes was achieved for continuous trivalent network decorated with dielectric walls of a certain width.[7,8] The HuD network structures used in this study were designed by employing centroidal tessellations of hyperuniform point patterns to generate a "dual" lattice, a connected network structure whose vertices were trihedrally coordinated.[7] The protocol for generating these networks proceeded by Delaunay's triangulating the hyperuniform point pattern and then connecting the center of mass of each of the elements in the triangulation to form polygonal cells. By construction, the dual-lattice vertices were trihedrally coordinated. The sides of the network cells were then decorated with dielectric walls, whose width was them varied to achieve the largest photonic gap for a given index contrast.

Sample Fabrication: The sample was grown by molecular beam epitaxy on a GaAs (001) wafer and consisted of two GaAs membranes separated by a $Al_{0.7}Ga_{0.3}As$ sacrificial layer, on top of a $Al_{0.7}Ga_{0.3}As$ sacrificial layer.[30,32] High-density InAs quantum dots (QDs) were embedded in the middle of the upper membrane, and act as optically active medium. The HuD structure was defined by electron-beam lithography, reactive-ion etching, and subsequent selective etching of the sacrificial layers. The slab thickness and the inter-membrane separation distance were extrapolated from the SEM analysis and were found to be $t = 130$ nm and $d = 105$ nm, respectively (details of the SEM investigation are given in Figure S4, Supporting Information). When using a double-membrane system, the symmetry of the problem leads to the splitting into symmetric and antisymmetric modes, which were vertically delocalized over the two membranes. It was theoretically and experimentally proven that the coupled modes displayed by double-membrane photonic systems inherit the in-plane spatial distributions of the original single-membrane uncoupled modes.[44]. Here, the focus was on antisymmetric solutions.

Numerical Simulations: For 2D HuD photonic structures generated under periodic boundary condition in a square of side L, $a = L/\sqrt{N}$ was as a characteristic length scale such that all patterns have point density $1/a^2$. The photonic bandstructure was calculated using the eigenmode expansion software MPB[27] for a supercell of side $a\sqrt{N}$ using the associated high symmetry points of the resulting Brillouin zone (of characteristic size $2\pi/(a\sqrt{N})$. 3D FDTD simulations were performed by using the commercial software Lumerical,[45] where a double-membrane system patterned with the HuD design (Figure 1a) was illuminated by an external, broadband planewave laterally incident on one edge of the structure; a frequency-domain monitor measured the transmitted power spectrum on the opposite side of the structure, normalized against the power injected by the source. 3D FEM simulations were performed by using the commercial software Comsol[46]; the double-membrane structure was simulating one membrane and by imposing perfect electric conductor (PEC) conditions in the plane between the two membranes, in order to detect antisymmetric solutions. More details can be found in Section S7, Supporting Information. The FEM result reported in Figure 5e was obtained by patterning the membranes with the nominal design of Figure 1a, while the FEM data in Figures 3 and 5f were given by the simulation of a design generated by the SEM top view image of Figure 3a (the description of the process can be found in Section S7, Supporting Information). In all simulations an index of refraction of 3.4 was employed.

Experimental Set-Up Near-Field Hyperspectral Imaging: A commercial SNOM (Twinsnom, Omicron) in an illumination/collection geometry. The spatially resolved optical maps were recorded by scanning the probe tip over the sample at a fixed distance (few tens of nm). The sample was excited by a laser diode at 785 nm, both the excitation and the signal collection occur through the tip, then the collected signal was dispersed by a spectrometer and collected by a cooled InGaAs array. At every tip position, the entire spectrum of the sample was collected with a spectral resolution of 0.1 nm. Each SNOM tip collecting area, which had a lateral size of 250 nm was the estimated spatial resolution of our system.

Near-field PL intensity measurements constituted an indication of the location and extent of the photonic modes of the system, not their exact intensity distribution. In order to obtain intensity maps that reproduced in more detail the spatial profiles of the modes, a multi-Lorentzian peak fit was performed on every analyzed mode; from the results of the fit, performed in every pixel of the map, the amplitude map of the mode was constructed, together with the central wavelength and Q factor. The values of the IPR were obtained by using the fitted amplitude maps, considering the fitted amplitude as an evaluation of $|E(r)|^2$ in the two dimensions of the SNOM scan. A scaling factor of 1.5 was then applied (Section S6, Supporting Information) in order to compare the data with the theoretical IPR values (calculated in 3D). The error bars come from the propagation ΔIPR, estimated as the maximum deviation between the minimum and maximum acceptable values of the IPR obtained by changing the threshold of the fits. More details and other examples of fitted modes can be found in Section S5, Supporting Information.

Supporting Information

Supporting Information is available from the Wiley Online Library or from the author.

Acknowledgements

This research was founded by the EU H2020 FET-OPEN project NARCISO (ID: 828890). The authors acknowledge M. Abbarchi for fruitful discussions.

Open access funding provided by Universita degli Studi di Firenze within the CRUI-CARE Agreement.

Conflict of Interest

The authors declare no conflict of interest.

Data Availability Statement

The data that support the findings of this study are available from the corresponding author upon reasonable request.

© 2022 The Authors. Advanced Optical Materials published by Wiley-VCH GmbH

Keywords

disordered nanostructures, FDTD, hyperuniform disordered, near-field hyperspectral imaging, photonic materials

Received: November 25, 2021
Revised: January 14, 2022
Published online: February 27, 2022

[1] W. H. Koo, S. M. Jeong, F. Araoka, K. Ishikawa, S. Nishimura, T. Toyooka, H. Takezoe, *Nat. Photonics* **2010**, *4*, 222.
[2] M. Burresi, F. Pratesi, K. Vynck, M. Prasciolu, M. Tormen, D. S. Wiersma, *Opt. Express* **2013**, *21*, A268.
[3] S. Yu, C. W. Qiu, Y. Chong, S. Torquato, N. P. Yu, *Nat. Rev. Mater.* **2021**, *6*, 226.
[4] K. Vynck, R. Pierrat, R. Carminati, L. S. Froufe-Pérez, F. Scheffold, R. Sapienza, S. Vignolini, J. J. Sáenz, *arXiv:2106.13892*, **2021**.
[5] D. S. Wiersma, *Nat. Photonics* **2013**, *7*, *188*.
[6] S. Torquato, F. H. Stillinger, *Phys. Rev. E* **2003**, *68*, 041113.
[7] M. Florescu, S. Torquato, P. J. Steinhardt, *Proc. Natl. Acad. Sci. USA* **2009**, *106*, 20658.
[8] L. S. Froufe-Pérez, M. Engel, P. F. Damasceno, N. Muller, J. Haberko, S. C. Glotzer, F. Scheffold, *Phys. Rev. Lett.* **2016**, *117*, 053902.
[9] L. S. Froufe-Perez, M. Engelb, J. J. Sáenz, F. Scheffold, *Proc. Natl. Acad. Sci. USA* **2017**, *114*, 9570.
[10] J. Haberko, L. S. Froufe-Pérez, F. Scheffold, *Nat. Commun.* **2020**, *11*, 4867.
[11] S. John, *Phys. Rev. Lett.* **1987**, *58*, 2486.
[12] S. Tsitrin, E. P. Williamson, T. Amoah, G. Nahal, H. L. Chan, M. Florescu, W. Man, *Sci. Rep.* **2015**, *5*, 13301(R).
[13] W. Man, M. Florescu, K. Matsuyama, P. Yadak, G. Nahal, S. Hashemizad, E. Williamson, P. Steinhardt, S. Torquato, P. Chaikin, *Opt. Express* **2013**, *21*, 19972.
[14] W. Man, M. Florescu, E. P. Williamson, Y. He, S. R. Hashemizad, B. Y. C. Leung, D. R. Liner, S. Torquato, P. M. Chaikin, P. J. Steinhardt, *Proc. Natl. Acad. Sci. USA* **2013**, *110*, 15886.
[15] N. Muller, J. Haberko, C. Marichy, F. Scheffold, *Adv. Opt. Mater.* **2014**, *2*, 115.
[16] W. Zhou, Z. Cheng, B. Zhu, X. Sun, H. K. Tsang, *IEEE J. Sel. Top. Quantum Electron.* **2016**, *22*, 288.
[17] R. Degl'Innocenti, Y. D. Shah, L. Masini, A. Ronzani, A. Pitanti, Y. Ren, D. S. Jessop, A. Tredicucci, H. E. Beere, D. A. Ritchie, *Sci. Rep.* **2016**, *6*, 19325.
[18] M. Castro-Lopez, M. Gaio, S. Sellers, G. Gkantzounis, M. Florescu, R. Sapienza, *APL Photonics* **2017**, *2*, 061302.
[19] C. De Rosa, F. Auriemma, C. Diletto, R. Di Girolamo, A. Malafronte, P. Morvillo, G. Zito, G. Rusciano, G. Pescec, A. Sassoc, *Phys. Chem.* **2015**, *17*, 8061.
[20] O. Leseur, R. Pierrat, R. Carminati, *Optica* **2016**, *3*, 763.
[21] M. Florescu, P. J. Steinhardt, S. Torquato, *Phys. Rev. B* **2013**, *87*, 165116.
[22] T. Amoah, M. Florescu, *Phys. Rev. B* **2015**, *91*, 020201(R).
[23] A. Lagendijk, B. van Tiggelen, D. S. Wiersma, *Phys. Today* **2009**, *62*, 24.
[24] M. Filochea, S. Mayborodac, *Proc. Natl. Acad. Sci. USA* **2012**, *109*, 14761.
[25] G. J. Aubry, L. S. Froufe-Pérez, U. Kuhl, O. Legrand, F. Scheffold, F. Mortessagne, *Phys. Rev. Lett.* **2020**, *125*, 127402.
[26] R. D. Batten, F. H. Stillinger, S. Torquato, *J. Appl. Phys.* **2008**, *104*, 033504.
[27] S. G. Johnson, J. D. Joannopoulos, *Opt. Express* **2001**, *8*, 173.
[28] M. Florescu, S. Torquato, P. J. Steinhardt, *Appl. Phys. Lett.* **2010**, *97*, 201103.
[29] J. Joannopoulos, S. Johnson, J. Winn, R. Meade, *Photonic Crystals: Molding the Flow of Light*, 2nd ed., Princeton University Press, Princeton, NJ **2008**.
[30] M. Petruzzella, F. M. Pagliano, Ž. Zobenica, S. Birindelli, M. Cotrufo, F. W. M. van Otten, R. W. van der Heijden, A. Fiore, *Appl. Phys. Lett.* **2017**, *111*, 251101.
[31] M. Petruzzella, F. La China, F. Intonti, N. Caselli, M. De Pas, F. W. M. van Otten, M. Gurioli, A. Fiore, *Phys. Rev. B* **2016**, *94*, 115413.
[32] Ž. Zobenica, R. W. van der Heijden, M. Petruzzella, F. Pagliano, R. Leijssen, T. Xia, L. Midolo, M. Cotrufo, Y. Cho, F. W. M. van Otten, E. Verhagen, A. Fiore, *Nat. Commun.* **2017**, *8*, 2216.
[33] D. Balestri, M. Petruzzella, S. Checcucci, F. Intonti, N. Caselli, F. Sgrignuoli, F. W. M. van Otten, A. Fiore, M. Guriol, *Adv. Mater.* **2019**, *31*, 1807274.
[34] J. Dong, D. A. Drabold, *Phys. Rev. Lett.* **1998**, *80*, S0031.
[35] S. Imagawa, K. Edagawa, K. Morita, T. Niino, Y. Kagawa, M. Notomi, *Phys. Rev. B* **2010**, *82*, 115116.
[36] T. Yuan, T. Feng, Y. Xu, *Opt. Express* **2019**, *27*, 6483.
[37] K. Vahala, *Nature* **2003**, *424*, 839.
[38] P. Lalanne, W. Yan, K. Vynck, C. Sauvan, J. P. Hugonin, *Laser Photonics Rev.* **2018**, *12*, 1700113.
[39] Y. Akahane, T. Asano, B. Son, S. Noda, *Nature* **2003**, *425*, 944.
[40] S. Haroche, D. Kleppner, *Phys. Today* **1989**, *42*, 24.
[41] S. Noda, M. Fujita, T. Asano, *Nat. Photonics* **2007**, *1*, 449.
[42] O. U. Uche, F. H. Stillinger, S. Torquato, *Phys. Rev. E* **2004**, *70*, 046122.
[43] O. U. Uche, S. Torquato, F. H. Stillinger, *Phys. Rev. E* **2006**, *74*, 031104.
[44] N. Granchi, M. Petruzzella, D. Balestri, A. Fiore, M. Gurioli, F. Intonti, *Opt. Express* **2019**, *27*, 37579.
[45] *Lumerical 3D Electromagnetic Simulator* , https://www.lumerical.com/products/fdtd/.
[46] *COMSOL Multiphysics® v. 5.6., COMSOL AB Stockholm* , Sweden, www.comsol.com.

© 2022 The Authors. Advanced Optical Materials published by Wiley-VCH GmbH